NAVAL POSTGRADUATE SCHOOL

MONTEREY, CALIFORNIA

THESIS

SURFACE LAYER VARIABILITY OF OPTICAL TURBULENCE OBSERVED FROM A COASTAL LAND TOWER

by

Melissa N. JonMoore

June 2023

Thesis Advisor: Qing Wang
Second Reader: Jesus Ruiz-Plancarte

THIS PAGE INTENTIONALLY LEFT BLANK

REPORT DOCUMENTATION PAGE	*Form Approved OMB No. 0704-0188*

1. AGENCY USE ONLY *(Leave blank)*	**2. REPORT DATE** June 2023	**3. REPORT TYPE AND DATES COVERED** Master's thesis

4. TITLE AND SUBTITLE
SURFACE LAYER VARIABILITY OF OPTICAL TURBULENCE OBSERVED FROM A COASTAL LAND TOWER

5. FUNDING NUMBERS

6. AUTHOR(S) Melissa N. JonMoore

7. PERFORMING ORGANIZATION NAME(S) AND ADDRESS(ES)
Naval Postgraduate School
Monterey, CA 93943-5000

8. PERFORMING ORGANIZATION REPORT NUMBER

9. SPONSORING / MONITORING AGENCY NAME(S) AND ADDRESS(ES)
N/A

10. SPONSORING / MONITORING AGENCY REPORT NUMBER

11. SUPPLEMENTARY NOTES The views expressed in this thesis are those of the author and do not reflect the official policy or position of the Department of Defense or the U.S. Government.

12a. DISTRIBUTION / AVAILABILITY STATEMENT
Approved for public release. Distribution is unlimited.

12b. DISTRIBUTION CODE
A

13. ABSTRACT (maximum 200 words)

This research addresses the temporal and vertical variability of small-scale turbulence in the coastal environment represented by the structure function parameter for the index of refraction, C_n^2, used to quantify the impact of atmospheric turbulence on electromagnetic and electro-optical wave (EM/EO) propagation through atmospheric scintillation. The measurements were made on a coastal 12-m scaffold tower during the Coastal Land-Air-Sea Interaction (CLASI) field campaigns in Monterey Bay, California, from June to October 2021. The results from this research show a diurnal variability of C_n^2 unique to the coastal region and the impact of wind direction associated with sea breeze/land breeze circulations. The results also reveal the vertical variations in C_n^2 seen from the three measurement levels on the tower and how such variability changes diurnally. The vertical variation was also found to be affected by the mean wind direction, particularly for the water vapor contribution to the total C_n^2.

14. SUBJECT TERMS optical turbulence, unmanned aerial system, UAS, refractive index, optical scintillation, Cn2, electromagnetic, electro-optical wave, EM/EO, Coastal Land-Air-Sea Interaction, CLASI	**15. NUMBER OF PAGES** 47
	16. PRICE CODE

17. SECURITY CLASSIFICATION OF REPORT	**18. SECURITY CLASSIFICATION OF THIS PAGE**	**19. SECURITY CLASSIFICATION OF ABSTRACT**	**20. LIMITATION OF ABSTRACT**
Unclassified	Unclassified	Unclassified	UU

NSN 7540-01-280-5500

Standard Form 298 (Rev. 2-89)
Prescribed by ANSI Std. 239-18

THIS PAGE INTENTIONALLY LEFT BLANK

Approved for public release. Distribution is unlimited.

SURFACE LAYER VARIABILITY OF OPTICAL TURBULENCE OBSERVED FROM A COASTAL LAND TOWER

Melissa N. JonMoore
Lieutenant Commander, United States Navy
BS, University of Texas, Permian Basin, 2008

Submitted in partial fulfillment of the
requirements for the degree of

MASTER OF SCIENCE IN METEOROLOGY AND PHYSICAL OCEANOGRAPHY

from the

NAVAL POSTGRADUATE SCHOOL
June 2023

Approved by: Qing Wang
Advisor

Jesus Ruiz-Plancarte
Second Reader

Wendell A. Nuss
Chair, Department of Meteorology

THIS PAGE INTENTIONALLY LEFT BLANK

ABSTRACT

This research addresses the temporal and vertical variability of small-scale turbulence in the coastal environment represented by the structure function parameter for the index of refraction, C_n^2, used to quantify the impact of atmospheric turbulence on electromagnetic and electro-optical wave (EM/EO) propagation through atmospheric scintillation. The measurements were made on a coastal 12-m scaffold tower during the Coastal Land-Air-Sea Interaction (CLASI) field campaigns in Monterey Bay, California, from June to October 2021. The results from this research show a diurnal variability of C_n^2 unique to the coastal region and the impact of wind direction associated with sea breeze/land breeze circulations. The results also reveal the vertical variations in C_n^2 seen from the three measurement levels on the tower and how such variability changes diurnally. The vertical variation was also found to be affected by the mean wind direction, particularly for the water vapor contribution to the total C_n^2.

THIS PAGE INTENTIONALLY LEFT BLANK

TABLE OF CONTENTS

THIS PAGE INTENTIONALLY LEFT BLANK

LIST OF FIGURES

LIST OF TABLES

THIS PAGE INTENTIONALLY LEFT BLANK

LIST OF ACRONYMS AND ABBREVIATIONS

AL	Aquaculture Lab
ASIS	Air-Sea Interaction Spar
CLASI	Coastal Land Air-Sea Interaction
COAMPS	Coupled Ocean-Atmosphere Mesoscale Prediction System
DOD	Department of Defense
ED	evaporative duct
EM	electromagnetic
EM-Line	electromagnetic sensor array
EO	electro-optical
HEL	high-energy laser
HELWS	high-energy laser weapon system
I-SPAR	inner shelf spar
IQR	inter-quartile range
MLML	Moss Landing Marine Laboratory
MOST	Monin-Obukhov Similarity Theory
NAVSLaM	Navy Atmospheric Vertical Surface Layer Model
ONR	Office of Naval Research
qT-ASIS	water vapor and temperature recording ASIS buoys
TKE	turbulent kinetic energy
UAS	unmanned aerial system

THIS PAGE INTENTIONALLY LEFT BLANK

ACKNOWLEDGMENTS

First and foremost, I would like to thank my advisor Dr. Qing Wang for embracing this topic and inspiring me to deep dive into boundary layer turbulence. Qing, your enthusiasm on boundary layer propagation is contagious and very motivating, thank you. I would also like to thank my second reader, Jesus Ruiz-Plancarte, Ryan Yamaguchi, and Mike Cook for entertaining my questions and assisting with my coding through this process. A special thank you to Brigadier General Annemarie Anthony and the JEMSO team at USSTRATCOM for first sparking my interest in the complex problem of electromagnetic spectrum operations.

My sincerest gratitude to Rob, Layla and Bobby for embarking and supporting me on this journey here in Monterey. I appreciate your continued sacrifice and understanding of having a wife and mother who consistently spent evenings working, running code, and on late night zoom calls. Thank you to my Navy cohort for your encouragement during the tough times and your joy and comradery that made the good times even better. Finally, thank you to Commander Tellado, NPS faculty and staff, and Naval Oceanography for recognizing the value of investing in our professional development and what it provides to the Fleet.

THIS PAGE INTENTIONALLY LEFT BLANK

I. INTRODUCTION

Over the past two decades the Department of Defense (DOD) has focused on advancing its high-energy laser weapon technology. In 2014, the Navy took delivery of the AN/SEQ-3 Laser Weapon System and then further advanced its employment capabilities with the implementation of adaptive optics. While advancements in technology and hardware can lead to an advantage over our adversaries, understanding how the environment, specifically the atmospheric boundary layer, will affect electro-optic (EO) propagation will further enhance our tactical advantage. The ability to exploit the environment for more efficient utilization of High Energy Laser Weapon Systems (HELWS) is supported by the National Defense Strategy's outline of enduring advantages (Department of Defense 2022).

The atmospheric boundary layer is the lowest portion of the atmosphere with the presence of turbulence where variations in the index of refraction cause scintillation of optical and microwave propagation signals. As such, atmospheric scintillation affects applications over a broad range of wavelengths of the electromagnetic waves (EM) such as in the performance of HELWS, electro-optical and infrared (EO/IR) sensors, free-space optical (FSO) links, and radio frequency (RF) propagations operating in the atmosphere. The turbulent variability of temperature and humidity within the lower atmospheric boundary layer is a poorly modeled and predicted area. The process is further complicated by differences in temperature and humidity mixing dynamics between land, sea, and its coastal interface. This topic has yet to be addressed since many of the HELWS testing and EO/IR sensor deployments occur near the coast. The Coastal Land-Air-Sea Interaction (CLASI) project sponsored by the Office of Naval Research (ONR) intends to address the challenges of forecasting the unique coastal environment using current operational numerical weather prediction systems such as the U.S. Navy's Coupled Ocean–Atmosphere Mesoscale Prediction System (COAMPS) (Haus et al. 2022).

The structure function parameter for the index of refraction (C_n^2) is a key variable used to quantify temperature and humidity perturbations within the atmospheric boundary layer affecting scintillation. The ability to accurately measure and predict how the

atmosphere will impact optical propagation from its source to the target is crucial to efficiently utilize HELWS engagements. Much of the previous research focused on quantifying the variations of C_n^2 at a single level, in both marine and inland environments. However, the vertical variability of C_n^2 close to the surface is significant and any slant path engagements of the optical systems would experience such vertical variation. The vertical variability of C_n^2 has not been well understood or modeled. In 2021, CLASI Monterey Bay conducted two phases of field campaigns deploying various buoys, a research aircraft, small research vessels, and many coastal land towers. One of the towers, EM0 at the Aquaculture Lab (AL) of Moss Landing Marine Lab (MLML), was installed at the coast and continuous measurements were made at three levels for about four months. This research uses the data collected from this tower and focuses on assessing the temporal and vertical variability of the C_n^2 in the complex coastal environment. We will focus on C_n^2 in the electro-optical (EO) wavelengths.

The objective of this research is to quantify optical turbulence in the coastal environment with the ultimate goal of improving environmental predictions in support of HELWS operations. Subjects to be addressed include the vertical variability of C_n^2 near the surface, the temporal variability of the C_n^2 profile at the coastline, and the relative contribution of temperature and water vapor to C_n^2 in a coastal environment. These subjects help build a deeper understanding of the lower marine boundary layer turbulence structure and its vertical variation for slant path HELWS engagements and other relevant applications.

II. BACKGROUND

Atmospheric turbulence has a profound impact on electromagnetic (EM) and electro-optical (EO) wave propagation. Turbulence is driven by shear and buoyancy fluctuations within the boundary layer. The flux Richardson number measures the dynamic stability of the layer:

$$R_f = \frac{\left(\frac{g}{\theta_v}\right)\left(\overline{w'\theta_v'}\right)}{\left(\overline{u'w'}\right)\frac{\delta \bar{U}}{\delta z}+\left(\overline{v'w'}\right)\frac{\delta \bar{V}}{\delta z}} \tag{1}$$

where g is acceleration due to gravity, $\overline{\theta_v}$ is the mean virtual potential temperature, $\overline{w'\theta_v'}$ is the kinematic buoyancy heat flux, $\overline{\mathrm{u'w'}}$ and $\overline{\mathrm{v'w'}}$ are momentum flux east-west (u) and north-south (v) wind components, $\frac{\delta \bar{U}}{\delta \mathrm{z}}$ and $\frac{\delta \bar{V}}{\delta \mathrm{z}}$ make up vertical wind shear components. When $R_f < 1$, the air is dynamically unstable, and turbulence is enhanced. For $R_f > 1$, the layer is dynamically stable and turbulence decays (Stull 1988).

Boundary layer turbulence shows clear diurnal variability, especially overland. During the day, a deep turbulent layer forms from increased surface kinematic heat flux and evaporation. After sunset, radiative cooling gives rise to a much cooler surface which results in negative surface heat flux and hence a stable boundary layer much lower than the daytime convective boundary layer. The remaining daytime mixed layer above the shallow stable boundary layer becomes the residual layer, a shallow neutral layer that has lost its turbulent kinetic energy source (Stull 1988). Within the residual layer turbulent eddies decay.

Turbulence eddies are generally classified by their scale into three regimes: the energy-containing eddies, the inertial subrange eddies, and the dissipation eddies (Kaimal et al. 1972). The energy-containing eddies are driven by surface heat and momentum fluxes that generate turbulent kinetic energy (TKE). The size of energy-containing eddies is dependent on multiple factors including the stability and depth of the boundary layer. These large eddies transfer energy into dissipation eddies through energy cascade across the inertial subrange. A typical energy density spectrum of turbulence is depicted in Figure 1.

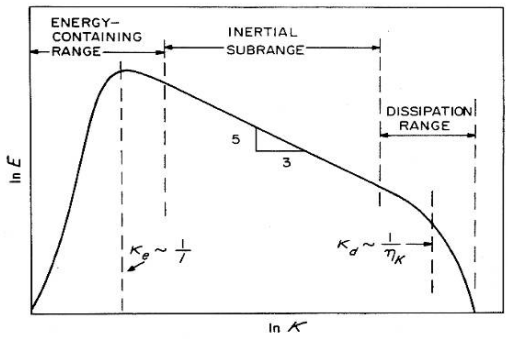

Figure 1. Schematic of turbulence energy spectra showing the three regimes of eddies in the boundary layer and the inertial subrange energy cascade with -5/3 law. Adapted from Stull (1988)

Dissipation eddies are the smallest eddies and define their length based on the Kolmogorov microscale (η):

$$\eta = \left(\frac{v^3}{\varepsilon}\right)^{1/4} \tag{2}$$

where v is the viscosity of the air, ε is the dissipation rate. Eddies of this scale dissipate TKE via molecular viscosity. Eddies within the inertial subrange follow the Kolmogorov inertial dissipation theory, experience energy spectra with a -5/3 relationship with wavenumber. Eddies of this size range have a significant impact on EO propagation through scintillation (Andrews 2019).

Atmospheric scintillation results in the fluctuation in phase and amplitude of EM waves due to perturbations in air density as EM waves travel through the atmosphere. The temperature and moisture perturbations in the inertial subrange are the source of perturbations in the refractive index (n) of moist air leading to scintillation, referred to as optical turbulence. Figure 2 illustrates scintillation effects in a turbulent environment when an EM wave propagates through the atmosphere. As optical signals propagate through the turbulent eddies, the phase speed will vary in response to the n gradients, resulting in refraction in accordance with Snell's Law (Stull 2000). The deformed wavefront at the target seen in Figure 2 is a result of the integrated refractive effects along the propagation path.

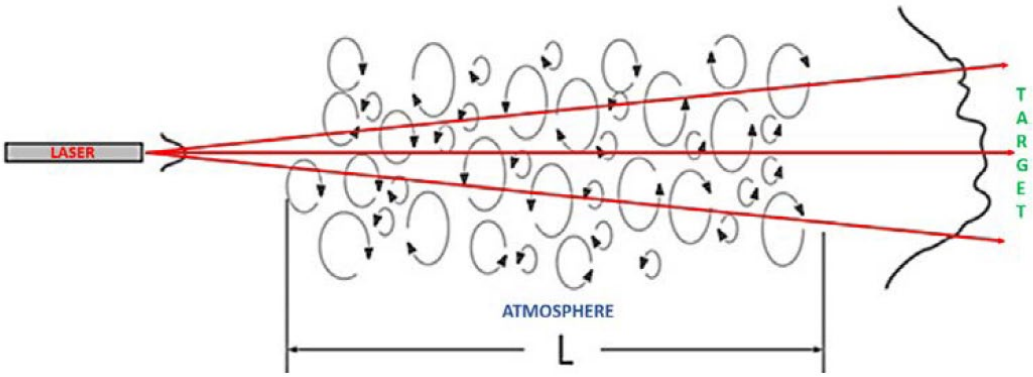

Figure 2. Schematic of turbulent atmosphere defocusing a laser beam wavefront. Adapted from Burger et al. (2008)

Atmospheric scintillation is quantified by the structure function parameter of the index of refraction denoted as C_n^2, which characterizes spatial coherence of *n* perturbations (Andrews and Phillips). It is based on the -5/3 law of the inertial subrange spectra and the corresponding -2/3 law of the structure function:

$$C_n^2 = \langle [n'^{(x)} - n'(x+r)]^2 \rangle r^{-\frac{2}{3}} \tag{3}$$

where x is a given point in space, r is the separation distance, n' is the perturbation of the index of refraction, and the quantity within the angular bracket is the structure function averaged over the spatial domain. Equation (3) can be used to calculate C_n^2 directly from the time/space domain (using Taylor's hypothesis when calculation is done in the temporal domain). C_n^2 can also be obtained in the spectral domain using the power spectrum in the inertial subrange,

$$\Phi_n(k_1) = 0.25 C_n^2 k_1^{-5/3} \tag{4}$$

where $\Phi_n(k_1)$ is the one-dimensional power spectrum of n, and k_1 is the wave-number component in stream-wise direction (Friehe et al. 1975).

Temperature and moisture are the causes of variability in the index of refraction. As such, the structure function parameter for *n* can be expressed in terms of the structure

parameters for temperature (C_T^2) and water vapor pressure (C_e^2) and their co-spectrum (C_{eT}) shown in Eq. (5) (Wyngaard 1971).

$$C_n^2 = B_1 C_T^2 + B_2 C_{eT} + B_3 C_e^2 \tag{5}$$

where B_1, B_2, and B_3 are weighting functions involving temperature and humidity and constants that vary with wavelength (Burk 1980). The three terms on the right-hand-side of Eq. (5) will be referred to as C_{nT}^2, C_{neT} , and C_{ne}^2. In a dry overland environment, C_n^2 can be simplified to be related to temperature structure parameter only (C_{nT}^2):

$$C_n^2 = (79 \times 10^{-6} P/T^2)^2 C_T^2 \tag{6}$$

where humidity contributions are considered negligible. Friehe et al. (1975) revealed humidity perturbations could not be neglected along a horizontal path in a marine environment and accurate C_n^2 calculations should include both temperature and humidity perturbations (Friehe et al. 1975; Wauer 2019).

Characteristics of structure function parameter in the surface layer can be parameterized following the Monin-Obukhov Similarity Theory (MOST):

$$C_T^2 = \theta_*^2 z^{-2/3} \phi_h(z/L)$$

$$C_{Tq} = r_{Tq} \theta_* q_* z^{-2/3} \phi_{hq}(z/L) \tag{7}$$

$$C_q^2 = q_*^2 z^{-2/3} \phi_q(z/L)$$

where L is the Obukhov length, $\phi_h, \phi_q, and\ \phi_{hq}$ are universal functions dependent on (z/L) for potential temperature, specific humidity and their cross-correlation, respectively (Foken 2006). The θ_* and q_* are the temperature and specific humidity scales defined from turbulent fluxes (Stull 1998). This theory requires assumptions of localized homogeneity and constant flux within the surface layer (Stull 1988), which has been found true for inland and marine atmospheric boundary layers (Wyngaard 1971; Friehe 1975). However, given the dynamic characteristics of the coastal boundary layer the same assumptions may not be valid (Wauer 2019).

The magnitude of C_n^2 varies significantly with time and space. The coastal area is a highly variable environment for the atmospheric boundary layer with two types of airmass due to their different adjacent surfaces: the land and the sea (Garratt 1992). An internal boundary layer is formed as one air mass is modified when it moves over a drastically different surface type often characterized by a change in surface roughness, heat capacity or moisture availability. (Stull 1988). The coastal area naturally has persistent internal boundary layers due to the land-sea contrasts (Stull 1988). At the mesoscale, this land-sea transition drives land/sea breeze circulation patterns caused by the differential surface heat capacity. Daytime heating over the land surface establishes an unstable surface layer, causing advection of the adjacent, moist marine boundary layer air onshore (Nuss 2003). At night, radiative cooling stabilizes the lower atmosphere on land over a mesoscale range of ~100 to 1000 km and drives downward vertical motion of the relatively dry land airmass. This process creates the land breeze phase and cool and dry air close to the surface is advected seaward (Stull 1988). There are diurnal variations of sensible heat flux overland and in the marine environment, but the magnitudes of variability are significantly smaller in the marine environment than over land (Stull 1988). Similarly, there are strong diurnal variations in C_n^2 overland with a somewhat different shape than those for sensible heat flux (Andrews 2019) where weak optical turbulence is generally found at sunrise and sunset during neutral stability conditions (Wesely and Alcaraz 1973). However, the diurnal variation of C_n^2 in the coastal zone has not been studied in the past. Optical turbulence is considered weak when $C_n^2 \leq 10^{-16}\left(m^{-2/3}\right)$ and strong when $C_n^2 \geq 10^{-13}\left(m^{-2/3}\right)$ (Andrews, 2019). Higher optical turbulence represents stronger impacts on optical signal propagation through scintillation.

THIS PAGE INTENTIONALLY LEFT BLANK

III. METHODOLOGY

The CLASI field campaign was conducted in Monterey Bay during the summer and fall of 2021 and 2022 and in Santa Rosa, Florida in winter of 2023 using instrumented Air-Sea Interaction Spar (ASIS) and Inner Shelf Spar (I-SPAR) buoys, a research aircraft, land towers, and remote sensing techniques to collect coupled air-sea measurements (Haus et all. 2022). During the 2021 campaign, an array of ASIS buoys extending approximately 30-km offshore and land towers extending 8-km inland from the Aquaculture Lab of MLML at (36.80098N, 121.789222W) were deployed to make continuous near-surface mean and perturbation measurements to characterize cross-shore variability of turbulence and mean meteorological conditions. The offshore portion of this array also measured electromagnetic wave propagation with the transmitters on the offshore buoys and receiver antenna arrays at the AL (Figure 3) (Haus et al. 2022). This EM-line utilized three specially outfitted ASIS buoys, referred to as qT-ASIS, with additional multi-level temperature, humidity, and wind sensors for near surface ocean profiling measurements. The land towers complete the cross-shore line with the central beach tower EM0, located approximately 20-m from the waterline, provided the data for this analysis.

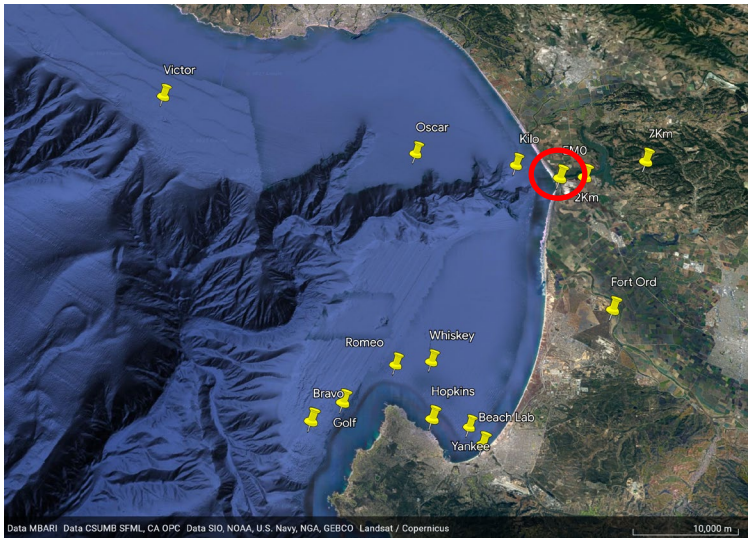

Figure 3. CLASI 2021 ASIS buoy and land tower placement in Monterey Bay with coastal tower EM0 (the push pin within the red circle) along the EM-Line (Victor to 7-km tower).

The EM0 measurements were collected from June to October 2021 during the CLASI Monterey Bay field campaign. EM0 is a 12-m scaffold tower instrumented at three levels with high-rate sensor packages collecting temperature, relative humidity, radiative fluxes, wind speed and direction, and concentrations of carbon dioxide (CO_2), and water vapor (H_2O) (Table 1). The high-rate flux sensor heights were located at 4.78-m, 8.62-m, and 11.86-m and will be referred to as the flux levels. The slow-sampling sensors for the mean variables were placed at five levels: 3.24, 4.88, 6.81, 8.73, and 11.54 m above the surface. A picture of the EM0 tower is shown in Figure 4.

Table 1. List of CLASI EM0 tower sensors (*data not used in this study).

Sensor	Sampling Rate	Height (m)	Measured variables
Gill Windmaster Pro	20 Hz	11.86	High-frequency 3-D wind components and sonic temperature
LICOR LI7500	40 and 20 Hz	11.86	High-frequency CO_2 density, H_2O density, and air pressure
Vaisala HUMICAP humidity and temperature probe HMP155	0.2 Hz	11.54, 8.73, 6.81, 4.88, 3.24	Air temperature and humidity
Outdoor Observation and Surveillance Field Camera	1 Hz	10.99	Images of sea state
*Droplet Measurement Technologies Fog Monitor FM-120	1 Hz	10, 5	Cloud particle spectrometer
Campbell Scientific temperature probe model 107	1 Hz	8.62, 4.94	Air temperature
Campbell Scientific Irgason	100 Hz	8.78, 4.78	High-frequency 3-D wind components, CO_2 density, H_2O density, and sonic temperature

Because of the proximity of the EM0 tower to the water line, measurements made from the coastal tower represent turbulence measurements that originate over the ocean

and are advected inland by the mean wind. The onshore wind direction is illustrated in Figure 4.

The EM0 tower data from CLASI 2021 was post-processed to include quality control (QC) and calculation of turbulent quantities such as turbulent fluxes of momentum, sensible and latent heat fluxes, turbulent kinetic energy, and components of C_n^2 (Eq. 3). The data QC included removal of apparent bad (outlier) data points and periods of known sensor issues. All turbulence variables were calculated using the turbulence perturbations within 20-min (long enough period to significantly reduce the random error of statistics) sliding windows without overlap.

Figure 4. Tower EM0 with all sensors. Onshore wind is illustrated in this figure to denote the orientation of the tower sensors.

Further processing of the derived products includes conditional sampling for categorizing the results under different wind conditions and obtaining composite diurnal variations. Although most of the meteorological data processing employs arithmetic averaging to get mean or variances, processing of C_n^2 requires further consideration because of the large range of variation of this quantity spanning nearly four orders of magnitude.

As a result, using mean or variance for statistics is not appropriate because the results are highly biased to the large values with very small percentage of occurrence. Figure 5 shows the differences in the composite diurnal variation of C_n^2. Figure 5 shows much higher C_n^2 at all three levels of measurements in the mean and the third measurement level shows a day/ night variability different from the two lower levels. The median, on the other hand, shows consistent variability in the composite diurnal variation. Hence, all statistics in C_n^2 will be shown using median or the inter-quartile range (IQR) in this study. The geometric mean displays similar behavior as the median (not shown).

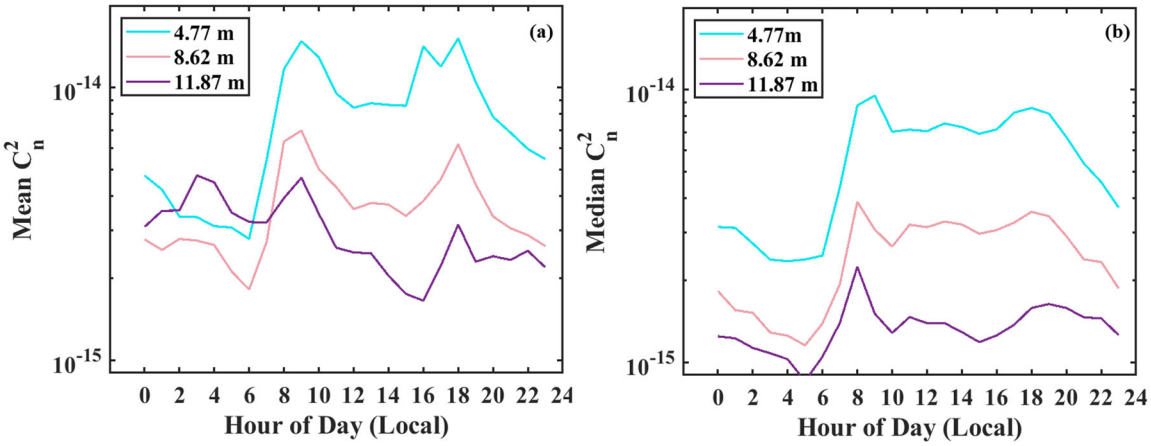

Figure 5. Comparison of mean (a) and median (b) composite C_n^2 diurnal variations using the entire EM0 dataset. A small number of significantly large C_n^2 values skewed the mean values in the nighttime hours.

IV. RESULTS

The land-based coastal tower was designed to record atmospheric surface layer turbulence variables at multiple levels to assess the variability of the coastal environment on turbulent properties including C_n^2 and the contribution of water vapor in C_n^2 calculations. This work discusses the results on C_n^2 found during the CLASI 2021 Monterey Bay field campaign. Figure 6 shows C_n^2 for the three flux levels on the tower and colored for the wind direction, depicting the overall variability of C_n^2 during the four months measurement period. Given the orientation of the coastline at MLML, the onshore wind is from around 270° (west, green/blue color) while the offshore winds nominally came from around 90° (east, pink/purple color). On the top level, the lowest C_n^2 was generally associated with the onshore flow, while the highest values were associated with the offshore flow. This trend is not as clear in the results from the two lower-level measurements, especially on the level closest to the surface. Because of the long period of the dataset, diurnal variability is not easily visualized in Figure 6, but it is much more apparent when focusing into shorter periods. Such diurnal variation is the strongest mode in the variability of C_n^2.

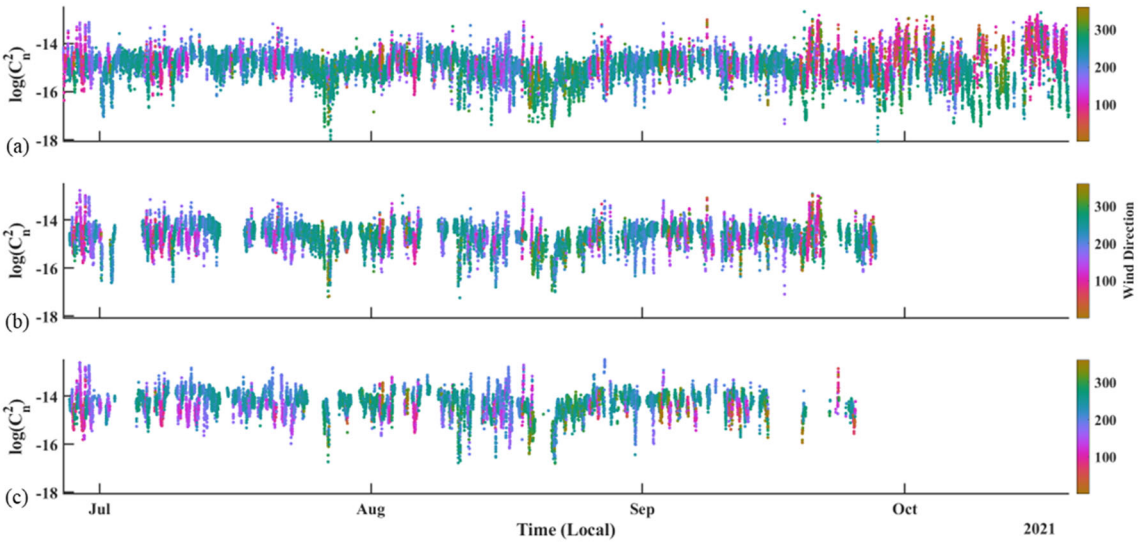

Figure 6. Temporal variations of C_n^2 from each flux level on the tower colored by wind direction. (a) – (c) are for the top, middle, and the bottom measurement levels, respectively.

Figure 7a shows the histogram of C_n^2 denoting the frequency of occurrence (FOC) of C_n^2 measured at all three flux levels. The magnitude of C_n^2 decreases with height while the range of variability increases toward the top sensors. Figure 7b shows the box-and-whisker plots for C_n^2 from all three measurement levels. It shows the same trend of decreasing C_n^2 where the median C_n^2 decreased to about 1/5 of its surface value with an altitude difference of only 7 m. In the following sections, C_n^2 will be further analyzed by three driving factors: vertical variability, diurnal variability, and wind-driven variability.

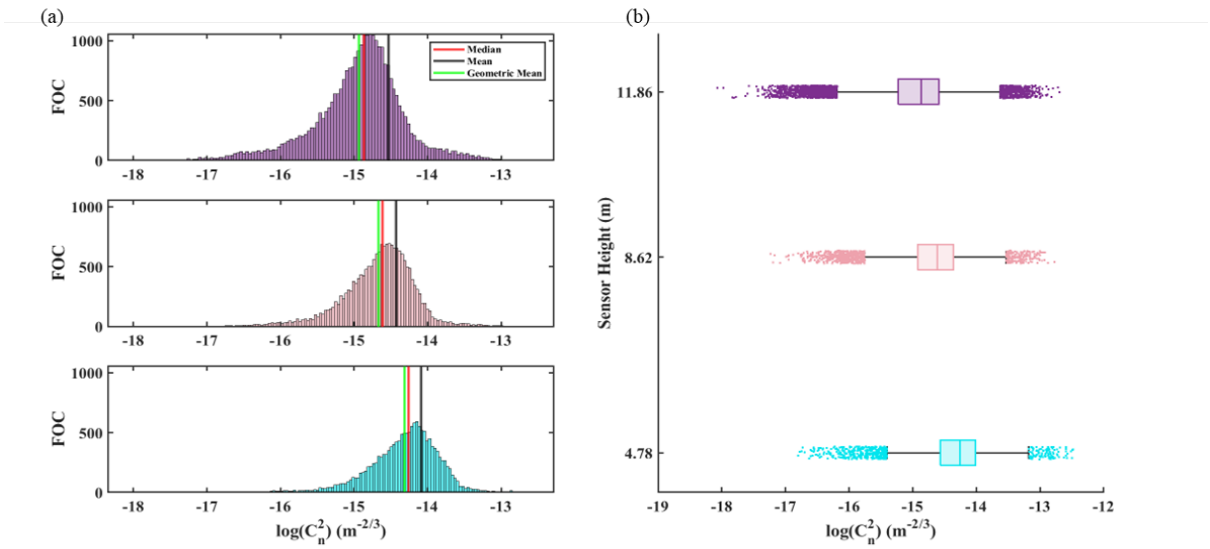

Figure 7. (a) FOC with associated median (red), mean (black) and geometric mean (green) and (b) box-and-whisker plots showing the median, quartiles, and outliers of C_n^2 obtained from the tower-based high frequency measurements. The three sub-panels (top to bottom) in (a) are results from each flux level on the EM0 tower at 11.86, 8.62, and 4.78 m, respectively.

A. VERTICAL VARIABILITY OF C_n^2

Analysis of C_n^2 across multiple time periods all indicate strong vertical variations as depicted in Figure 8 showing a short period of temporal variation at all three flux levels. We first noticed the similarity of the temporal variation at all three levels although the magnitude at the lowest measurement level was much higher than the two levels above. All three levels show consistent wind direction, although this is not always the case. This short time series also reveals the level of variability for C_n^2. Figure 8 shows increased variability of C_n^2 indicated by the increased scatter of data points from the surface to the top level.

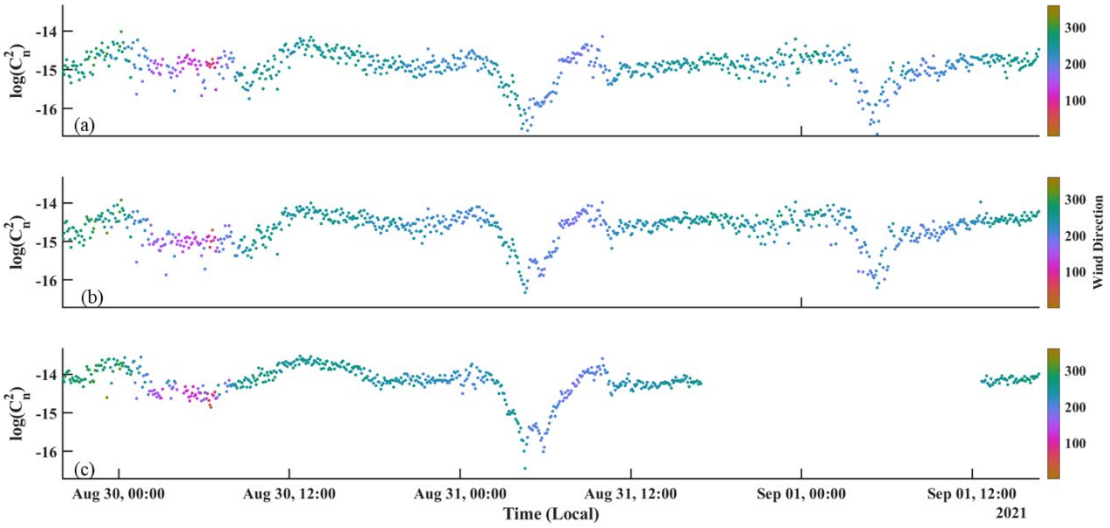

Figure 8. C_n^2 variability between Aug. 30 and Sept. 1, 2021.

B. DIURNAL VARIABILITY OF C_n^2

Similar to other turbulence quantities, C_n^2 shows strong diurnal variability near the surface over land with a peak around local noontime and decreases sharply at sunset and sunrise where the surface layer thermal stability transitions between stable and unstable stratifications (Wesely and Alcaraz 1973). Such diurnal variability was examined using the measurements from the coastal EM0 tower. Figure 9a shows the composite diurnal variations of the mean wind direction in degrees, where zero degrees denotes wind coming from the north). During daytime, all three measurement levels show very consistent wind direction as it veers from southerly to westerly in the morning hours after sunrise at ~0600 LST. Backing of mean wind occurs near noontime and reached south-south-westerly at midnight. The composite for C_n^2 is shown in Figure 9b. In the early morning hours, C_n^2 increases rapidly at all three levels until 0800 LST where a sudden decrease occurs. By around 1000 LST, C_n^2 levels off at its local minimum until 1500 LST. This time period of reduced C_n^2 corresponds to wind direction between 250 and 260° where there is the strongest sea breeze. Figure 9 suggests that the deviation from the sine-function like C_n^2 variability typically found over land is associated with the influence of the advected marine air during the sea breeze onshore flow. Furthermore, Figure 9 shows the large vertical

gradient in C_n^2 both at night and during day despite the marine air influence. Hence, the EM0 measurements depict a unique pattern of temporal variability in the coastal environment.

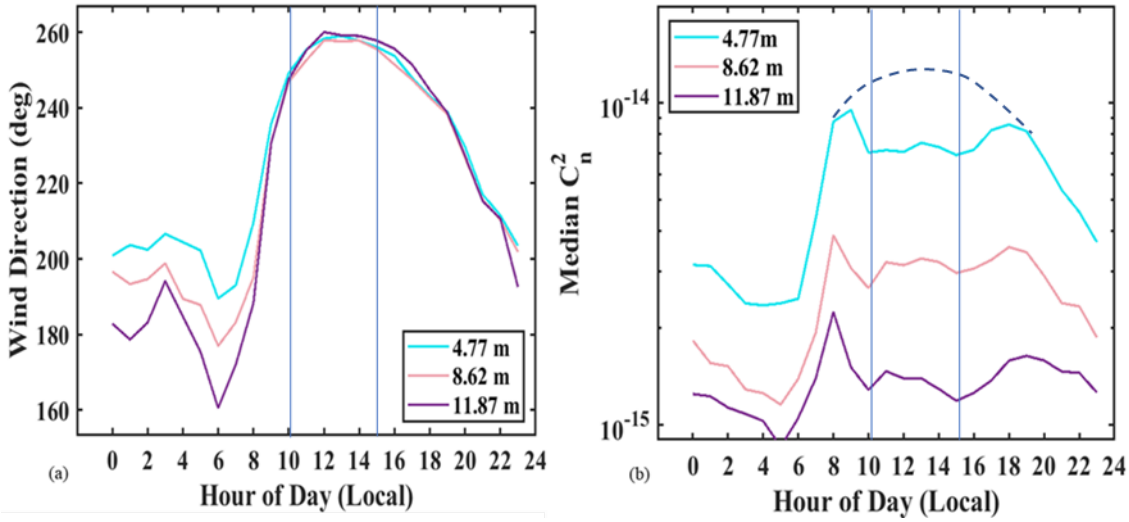

Figure 9. (a) Mean hourly wind direction. (b) Median hourly C_n^2. The two vertical lines on both subplots denote the period of local C_n^2 minimum from the advected marine air. The blue dash curve is an illustration of the expected C_n^2 variation for the lowest measurement level overland based on previous research.

C. WIND DRIVEN VARIABILITY OF C_n^2

Figure 10 uses two examples to corroborate the diurnal variability shown in the composite C_n^2 diurnal variation (Figure 9). Here, the C_n^2 values are again color-coded with wind direction to clearly illustrate the variability associated with the coastal mesoscale circulation. Figure 10a shows an example with clearly identifiable sea breeze and land breeze periods between 28 and 30 June 2021. On June 28, sea breeze started at 0915 and ended at 1735, while on 29 June, the sea breeze flow can be identified between 0930 and 1735 LST. The decrease of C_n^2 came immediately upon the onset of the sea breeze and ended abruptly as the sea breeze ends on both days. The difference between the C_n^2 values before and after the onset of sea breeze is approximated at $4 \times 10^{-14} m^{-2/3}$. Increased

variability is evident during the offshore or land breeze regimes illustrated by the spikes in warmer colors of Figure 10a. Although the nighttime C_n^2 have similar magnitudes as that during the daytime sea-breeze period, it shows significantly less small-scale temporal variability compared to the daytime sea breeze regime.

The coastal land and sea breeze circulations are not always apparent due to the predominant synoptic flow, as seen in Figure 10b. During periods of prolonged onshore flow, C_n^2 still showed some influence of the 'land breeze' effect with reduced C_n^2 around the time period of expected land-breeze (shaded area in Figure 10b). The nighttime cooling overland weakened the persistent onshore wind and, thus, the C_n^2 was mostly affected by the local land surface. Although this explanation is physically plausible, it requires more cases to validate.

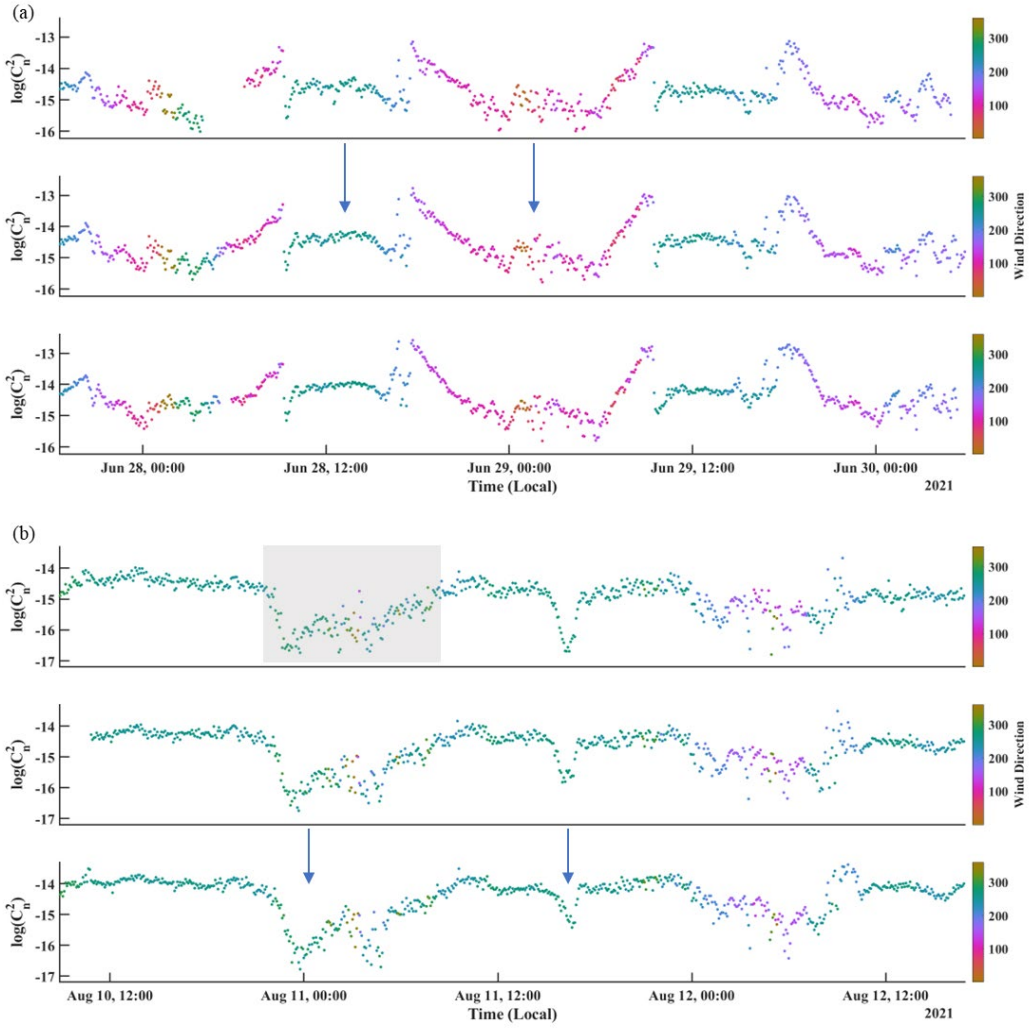

Figure 10. (a) Sea/land breeze-induced variation of C_n^2 with increased C_n^2 at wind transitions and during periods of offshore flow. (b) Period of continuous synoptic onshore flow with mesoscale sea/land breeze variability signature (shaded in gray). In both (a) and (b), the top panels are for the highest measurement level.

Figure 11 shows another example of large-scale coastal dynamics affecting the nominal diurnal variability of C_n^2. During a fall heat wave event in Monterey Bay from 15–17 October, significant heating resulted in predominantly offshore flow with shortened sea breeze periods. C_n^2 measurements remained elevated during this period and abrupt temperature drops of nearly 15 degrees Celsius were observed at the transition to sea breeze (Figure 11 a-b). On both 15 and 16 October, recovery of C_n^2 from the early morning neutral

event extended until about 1315 (15 Oct) and 1300 (16 Oct) when C_n^2 reached to a maximum of $1.59 \times 10^{-13} m^{-2/3}$, dropping by almost two orders of magnitude at the onset of the late sea breeze flow.

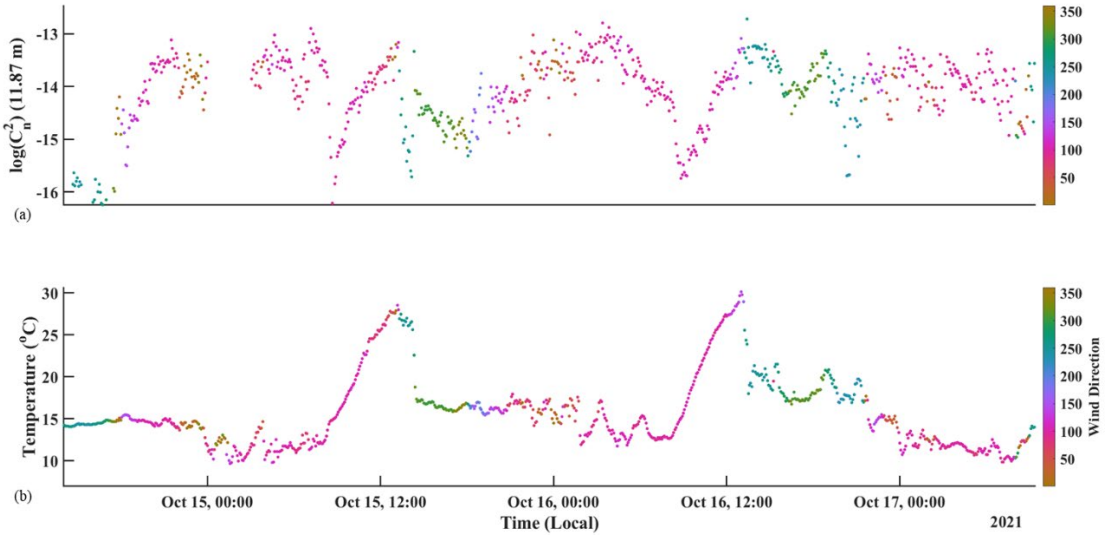

Figure 11. (a) C_n^2 and (b) temperature variability associated with the sea/land breezes during fall heat wave events.

D. TEMPERATURE AND WATER VAPOR CONTRIBUTION TO C_n^2

The contribution of temperature and water vapor to C_n^2 has been discussed in some literature (e.g., Burk 1980, Friehe et al. 1975). In his overland simulation, Burk (1980) found negligible contributions from water vapor so that Eq. 4 is an accurate depiction of C_n^2 (Burke 1980). Ingram (2017) analyzed aircraft-based measurements on the U.S. East coast and identified ~18% contribution to C_n^2 through the cross-correlation term between temperature and humidity (Ingram 2017). This topic is further investigated here using coastal measurements. We use the ratio of each of the three terms on the right-hand-side of Eq. (5) to the total C_n^2 to illustrate the importance of the terms. Figure 12 illustrates these ratios for the entire measurement period and for a few special cases. In most cases, the water vapor contribution (C_e^2) is less than 2% of the total C_n^2 and could be neglected without significant impacts to overall C_n^2 magnitude (Figure 12a). However, when there is a

decrease in temperature contribution from C_T^2 to the same order of magnitude as that ignoring C_{ne}^2, or the water vapor contribution, cannot be justified. In this case, contributions from C_e^2 rises to near 50% of the total C_n^2 (Figure 12 c-d). Figure 12 also suggests that C_{eT} in general has larger magnitude than C_{ne}^2 although it may change to negative in stable conditions. The positive contribution of C_{eT} to C_n^2 is nominally less than 2%.

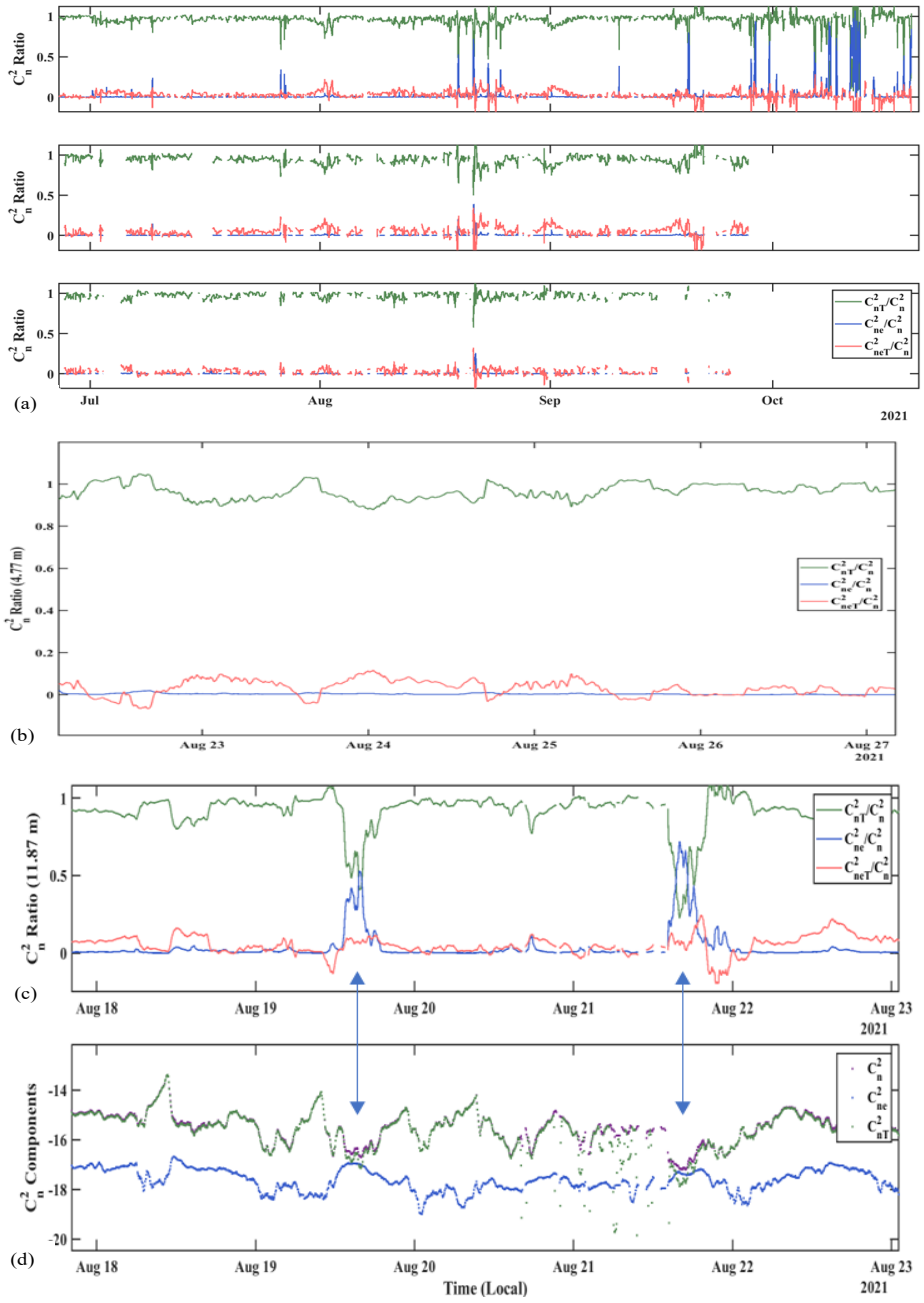

Figure 12. Component contributions to C_n^2. (a) The ratio of contributions of temperature (C_{nT}^2), water vapor (C_{ne}^2), and the cross-correlation of temperature and water vapor (C_{neT}) to C_n^2; (b) Same as in (a), except zoomed in to a 'normal' period between 23 and 27 August; (c) Same as in (a) except for a time period with a sharp decrease of (C_T^2); and (d) same as in (c) except C_{nT}^2 and C_{ne}^2 are plotted instead of their ratio to C_n^2.

V. SUMMARY AND CONCLUSIONS

Advancement and optimization of the HELWS is a major interest for the United States military. In order to optimally utilize these weapon systems, it is imperative to understand and accurately predict the affects optical turbulence in the operational environment.

In this work, we used coastal tower-based measurements to evaluate the variability of C_n^2 within the lowest 12-m of the coastal atmospheric boundary layer. The measurements were part of the CLASI 2021 field campaign from June to October 2021. The analyses focused on the vertical variability, diurnal variability, and wind regime dependence of C_n^2, and the contribution of temperature and water vapor to C_n^2 within the coastal environment. We identified that the vertical variability of C_n^2 increased with height while overall C_n^2 measurements decreased with height. The impact of diurnal variation further influences optical turbulence. The diurnal cycle causes an increase in C_n^2 during daytime heating but the onset of the sea breeze and advection of the moist marine atmosphere created two-separate C_n^2 maxima that is unique to the coastal environment. We also identified increased C_n^2 variability at the sea and land breeze transitions even when the synoptic scale flow did not result in a true sea or land breeze regime. During extreme heating events elevated C_n^2 is indicative of enhanced uncertainty in optical propagation. Finally, we identified that C_n^2 calculations in the coastal environment are similar to those in an inland dry environment and the contributions of C_{ne}^2 is significantly less than that of C_T^2 and can be neglected in most cases. The exception to this is when there is a substantial drop in C_T^2 to the same order of magnitude as the C_{ne}^2 where the water vapor contribution increases and cannot be neglected.

These findings emphasize the importance of understanding the complex coastal environment for the horizontal and slant path EO propagation of HELWS. Accurate collection, modeling, and prediction of the coastal atmospheric boundary layer and optical turbulence is critical for optimum sensor performance.

THIS PAGE INTENTIONALLY LEFT BLANK

VI. FUTURE WORK

Evaluation and validation of UAS mounted high-rate sensors for collecting in-situ measurements of the operational coastal and marine environment for incorporation into high energy laser weapon performance prediction decision aids. Validation of these sensors would provide operators with real-time optical turbulence calculations in dynamic environments often not resolved by numerical weather models.

THIS PAGE INTENTIONALLY LEFT BLANK

LIST OF REFERENCES

Andrews, L. C., 2019: *Field Guide to Atmospheric Optics.* 2nd ed., SPIE Press. 185 pp.

Burger, L., I.A. Litvin, and A. Forbes, 2008: Simulating atmospheric turbulence using a phase-only spatial light modulator. *S. Afr. J. Sci.,* **104**, 129–134, http://www.scielo.org.za/pdf/sajs/v104n3-4/a1110404.pdf (Accessed August 20, 2022).

Burk, S., 1979: Refractive Index Structure Parameter: Time-Dependent Calculating Using a Numerical Boundary-Layer Model. *J. Appl. Meteor. Climatol., **19***, 562–576, http://journals.ametsoc.org/doi/abs/10.1175/1520-0450(1980)019%3C0562%3ARISPTD%3E2.0.CO%3B2.

Department of Defense, 2022: *National Defense Strategy.* Department of Defense, Washington, D.C., https://media.defense.gov/2022/Oct/27/2003103845/-1/-1/1/2022-NATIONAL-DEFENSE-STRATEGY-NPR-MDR.PDF (Accessed August 1, 2022).

Friehe, C. A., J. C. La Rue, F. H. Champagne, C. H. Gibson, and G. F. Dreyer, 1975: Effects of temperature and humidity fluctuations on the optical refractive index in the marine boundary layer. *J. Opt. Soc. Amer.,* **65**, 1502, https://doi.org/10.1364/JOSA.65.001502.

Garratt, J. R., 1992: *The Atmospheric Boundary Layer*. Cambridge University Press. 316 pp. https://doi.org.10.1002/qj.49712051919.

Haus, T., Ortiz-Suslow, D. G., Doyle, J. D., Flagg, D. D., Graber, H. C., MacMahan, J., Shen, L., Wang, Q., Willams, N. J., & Yardim, C., 2022: CLASI: Coordinating Innovative Observations and Modeling to Improve Coastal Environmental Prediction Systems. *Bull Amer. Meteor. Soc.*, **103**(3), E889–E898. https://doi.org/10.1175/BAMS-D-20-0304.1.

Ingram, A. J., 2017: Quantifying factors affecting optical turbulence propagation using a controlled towed vehicle from an aircraft. M. S. thesis, Dept. of Meteorology, Naval Postgraduate School, 58 pp. https://calhoun.nps.edu/handle/10945/56733.

Kaimal, J. C., Wyngaard, J. C., Izumi, Y., & Coté, O. R., 1972: Spectral characteristics of surface-layer turbulence. *Q. J. Roy. Meteor. Soc., **98***(417), 563–589. https://doi.org/10.1002/qj.49709841707.

Nuss, W. A., 2003: Course notes for MR 4240: Coastal Meteorology Chapter 1 Introduction, 13 pp.

Stull, R. B., 1988: *An Introduction to Boundary Layer Meteorology*. Springer, Netherlands, 670 pp.

Stull, R. B. and Ahrens, C. D., 2000: *Meteorology for scientists and engineers*. 2nd ed., Brooks/Cole, 502 pp.

Wauer, B. J., 2019: Optical turbulence in the coastal marine environment and its impact on high energy laser weapon performance. Ph.D. dissertation, Dept. of Meteorology, Naval Postgraduate School, 228 pp.

Wesely, M.L. and Alcaraz, E.C., 1973: Diurnal cycles of the refractive index structure function coefficient. *J. Geophys. Res.,* **78**, 6224, https://doi.org/10.1029/JC078i027p06224.

Wyngaard, J. C., Y. Izumi, and J. Collins, 1971: Behavior of the refractive-index structure parameter near the ground. *J. Opt. Soc. Am.,* **61**, 1646–1650, https://doi.org/10.1364/JOSA.61.001646.

INITIAL DISTRIBUTION LIST

1. Defense Technical Information Center
   Ft. Belvoir, Virginia

2. Dudley Knox Library
   Naval Postgraduate School
   Monterey, California